lubricants

MDPI

Article

Tribo-Catalytic Degradation of Methyl Orange Dye via Cu/Al_2O_3 Nanoparticles

Claudia Cirillo [1,2,*], Mariagrazia Iuliano [1,2], Sana Abrar [1,3], Elena Navarrete Astorga [4] and Maria Sarno [1,2]

[1] Department of Physics "E.R. Caianiello", University of Salerno, Via Giovanni Paolo II, 132, 84084 Fisciano, SA, Italy
[2] Centre NANO_MATES, University of Salerno, Via Giovanni Paolo II, 132, 84084 Fisciano, SA, Italy
[3] University School for Advanced Studies IUSS Pavia, 27100 Pavia, PV, Italy
[4] Laboratorio de Materiales y Superficies (Unidad Asociada al CSIC), Departamento de Física Aplicada I, Universidad de Málaga, E29071 Málaga, Spain
* Correspondence: clcirillo@unisa.it; Tel.: +39-089-964335

Abstract

In this study, we report, for the first time, the tribo-catalytic degradation of methyl orange (MO) using Cu/Al_2O_3 nanoparticles under mechanical stirring conditions. The hybrid catalyst was synthesized via a wet impregnation method and characterized through different techniques, confirming structural integrity and compositional uniformity. When subjected to friction generated by a PTFE-coated magnetic stir bar, Cu/Al_2O_3 nanoparticles exhibited high tribo-catalytic activity, achieving up to 95% MO degradation within 10 h under dark conditions. The observed activity surpasses that of alumina alone and is attributed to the synergistic effects between copper and alumina, facilitating charge separation and enhancing reactive oxygen species (ROS) formation. Tribo-catalytic efficiency was further influenced by stirring speed and contact area, confirming the key role of mechanical friction. Reusability tests demonstrated stable performance over five cycles, highlighting the material's durability and potential for practical environmental remediation applications.

Keywords: tribo-catalysis; Cu/Al_2O_3 nanoparticles; methyl orange; organic dye degradation; mechanical energy harvesting; reactive oxygen species; wastewater treatment; environmental remediation

check for updates

Received: 29 July 2025
Revised: 10 September 2025
Accepted: 14 September 2025
Published: 17 September 2025

Citation: Cirillo, C.; Iuliano, M.; Abrar, S.; Navarrete Astorga, E.; Sarno, M. Tribo-Catalytic Degradation of Methyl Orange Dye via Cu/Al_2O_3 Nanoparticles. *Lubricants* **2025**, *13*, 418. https://doi.org/10.3390/lubricants13090418

Copyright: © 2025 by the authors. Licensee MDPI, Basel, Switzerland. This article is an open access article distributed under the terms and conditions of the Creative Commons Attribution (CC BY) license (https://creativecommons.org/licenses/by/4.0/).

1. Introduction

In recent years, tribo-catalysis has attracted growing interest within the scientific community as an innovative and promising catalytic technology for the degradation of organic pollutants. It offers a sustainable and environmentally friendly approach by effectively converting mechanical energy, naturally present in the environment, into chemical energy capable of driving degradation reactions. This mechanical energy can originate from various ambient sources, such as vibrations [1], flowing water [2], or can be reproduced by artificial means, such as magnetic stirring [3,4]. Unlike conventional catalytic methods, such as photocatalysis [5–8] and piezocatalysis [9–13], which rely on light irradiation or structural deformation, tribo-catalysis operates through the tribo-electric effect. This physical phenomenon occurs when two materials of different natures come into contact and are then separated through a rubbing or frictional motion [2]. During this process, when two dissimilar materials come into contact and are subsequently separated through friction or mechanical movement, a transfer of electrons takes place between their surfaces [2]. This electron exchange results in an imbalance of electrical charges, causing one material

to become positively charged while the other becomes negatively charged [14]. As a consequence, significant surface charge accumulation occurs on both materials, laying the foundation for subsequent redox reactions when these charges interact with surrounding molecules, such as water and oxygen, in the environment.

These tribo-electric charges, once transferred into an aqueous medium, interact with water and dissolved oxygen to produce reactive oxygen species (ROS) [15], including hydroxyl radicals (·OH) and superoxide anions ($\cdot O_2^-$), which are capable of oxidizing and breaking down complex organic compounds into less harmful substances. Due to its simplicity, environmental compatibility [16], and ability to function under ambient conditions without external energy sources, tribo-catalysis presents a particularly attractive approach for wastewater treatment applications [16].

In this context, one of the most critical environmental challenges is the removal of synthetic azo dyes from industrial effluents [17,18], particularly methyl orange (MO) [19,20]. MO is an anionic dye widely employed in the textile, printing, and chemical industries, as well as in analytical applications as a pH indicator. Its molecular structure, featuring an azo bond (–N=N–) and substituted aromatic rings, imparts high chemical stability, low biodegradability, and strong resistance to conventional treatment methods [21,22]. Furthermore, MO is known to be toxic to aquatic life and potentially harmful to human health, necessitating the development of more effective and sustainable remediation strategies [23].

Tribo-catalysis, although still relatively new compared to photocatalysis and piezocatalysis, has been increasingly explored for environmental remediation. Advances in tribo-catalysis have demonstrated its potential in degrading dyes, antibiotics, and other persistent organic pollutants [15,16,22], thereby positioning it as a sustainable alternative within the broader field of advanced oxidation processes. Nonetheless, a comprehensive understanding of the mechanisms, active materials, and structure–activity relationships is still developing, and systematic investigations remain limited.

Previous studies have shown that semiconductor oxides such as TiO_2 [24], ZnO [25,26], $BiOIO_3$ [27], $CaCu_3Ti_4O_{12}$ [28], and CdS [29] can act as efficient tribo-catalysts due to their capacity to generate electron–hole pairs under mechanical stress and their robustness in aqueous environments. The catalytic performance of such materials can be significantly improved by using mixed oxides or bimetallic systems, which leverage synergistic interactions between components. In this regard, alumina (Al_2O_3) offers chemical stability [30], high thermal resistance [31], and a large specific surface area [32] conducive to the adsorption and distribution of reactive species [33]. Furthermore, its excellent insulating properties enhance charge accumulation on the catalyst surface. Copper (Cu), on the other hand, exhibits favorable redox characteristics [34] and can promote electron transfer [34] and radical formation during catalytic processes [35].

The combination of these two materials into a hybrid Cu/Al_2O_3 catalyst offers the potential for enhanced tribo-catalytic activity through improved charge generation, better electron–hole separation, and more efficient interaction with the target pollutant.

In this work, we investigated, for the first time, the tribo-catalytic performance of Cu/Al_2O_3 for the degradation of methyl orange under standard magnetic stirring conditions, employing a sealed polytetrafluoroethylene (PTFE) magnetic stir bar. The mechanical energy generated from the friction between the catalyst particles and either the magnetic stir bar or the bottom surface of the reaction vessel was effectively utilized to induce tribo-electric charge accumulation on the catalyst surface, thereby initiating oxidative degradation of the dye molecules. By varying the size of the stir bar and the material composition of the reaction container, the overall dye removal efficiency was further enhanced. Additionally, the stability and reusability of the Cu/Al_2O_3 catalyst were also evaluated.

2. Experimental

2.1. Materials

All reagents were purchased from Sigma-Aldrich (Darmstadt, Germany) and used as received without further purification. The chemicals employed in this study included α-Al_2O_3 (alpha-alumina, 99%), copper nitrate ($Cu(NO_3)_2$, 99.9%), deionized water, methyl orange (MO, dye content 85%), hydrochloric acid (HCl, 0.1 M), sodium hydroxide (NaOH, 0.1 M), p-Benzoquinone (BQ, >98%), tert-butanol (TBA, >99%), silver nitrate ($AgNO_3$, >99%), and ethylenediaminetetraacetic acid disodium salt dihydrate (EDTA-2Na, >99).

2.2. Synthesis

The copper catalyst supported by α-Al_2O_3 was synthesized by the wet impregnation technique, following the procedure described in [36], using α-Al_2O_3 characterized by a low specific surface area (0.57 sq. m/g) and negligible micropore volume (0.00 cub. mm/g). In a typical preparation, 300 mg of α-Al_2O_3 were dispersed in 20 mL of a 1 wt.% aqueous solution of copper nitrate ($Cu(NO_3)_2$). The suspension was continuously stirred for 2 h to ensure homogeneous impregnation. Subsequently, the solvent was removed using a rotary vacuum evaporator (Hei-VAP Core, Heidolph, Schwabach, Germany). The obtained material was dried overnight at 105 °C and then calcined in air at 500 °C for 3 h. The synthesis yield was 95.8 wt.% $\pm$ 1.2, with a reproducible copper loading of approximately 17 wt.% $\pm$ 2.7 in the form of Cu nanoparticles, as confirmed across three independent preparations.

2.3. Characterization of Cu/Al_2O_3 Nanoparticles

The Cu/Al_2O_3 catalysts were characterized using several analytical techniques to assess their structural, morphological, chemical, and thermal properties. X-ray diffraction (XRD) analysis was performed using a Bruker D2 Phaser diffractometer with Cu Kα radiation over a 2θ range of 10° to 80°, to determine the crystalline structure of the nanoparticles. FT-IR spectra were recorded using a Nicolet iS50 FT299 IR (Nicolet, Waltham, MA, USA). Raman spectra were obtained at room temperature with a microRaman spectrometer (Renishaw inVia; 514 nm excitation wavelength). The specific area and pore volume of α-alumina were obtained by N_2 adsorption–desorption at 77 K with a Kelvin 1042 V3.12, COSTECH Instruments (Costech Microanalytical, Tallinn, Estonia). The surface morphology and particle distribution were examined using Scanning Electron Microscopy (SEM) with a TESCAN VEGA LMH microscope operating at 230 V (Tescan, Brno, Czech Republic). The energy resolution of the detector was approximately 129 eV at Mn Kα. Additionally, a FEI Tecnai 20 Transmission Electron Microscope (TEM), operating at 200 kV with LaB_6 filament as the electron source, was employed for further characterization. X-ray Photoelectron Spectroscopy (XPS) was carried out using a Physical Electronics (PHI) VersaProbe II spectrometer equipped with an Al Kα radiation source to investigate the surface chemical composition and oxidation states of the elements.

2.4. Evaluation of Tribo-Catalytic Activity

The tribo-catalytic efficiency of Cu/Al_2O_3 nanoparticles was evaluated through the degradation of MO under magnetic stirring, performed in the dark and at room temperature. The concentration of MO was monitored by recording the absorption spectra using a UV–Vis spectrophotometer (Evolution 60S model). In a representative experiment, 50 mg of Cu/Al_2O_3 were dispersed in 30 mL of an aqueous MO solution with a concentration of 20 mg/L, contained in a glass beaker (75 mm in diameter, 95 mm in height). The suspension was stirred using a PTFE-coated cylindrical magnetic stir bar (∅ 8 mm $\times$ 35 mm) at a constant speed of 500 rpm under dark conditions. At regular intervals of 2 h, 3 mL aliquots

were collected and centrifuged at 10,000 rpm for 5 min to separate the solid catalyst. The degradation ratio was then calculated according to Equation (1) [37,38]:

$$\text{Degradation}(\%) = \frac{C_0 - C_t}{C_0} \cdot 100\% \quad (1)$$

where C_0 and C_t represent the initial concentration and the concentration at time t of MO, respectively.

3. Results and Discussion

3.1. Characterization of Nanoparticles

The XRD patterns of α-Al_2O_3 and Cu/Al_2O_3 samples are presented in Figure 1a, recorded over the 2θ range of 20–80°. The diffractogram of α-alumina (red line) shows sharp diffraction peaks at 2θ ≈ 25.6°, 35.1°, 37.8°, 43.3°, 52.5°, 57.5°, 66.5°, and 77.0° corresponding to the (012), (104), (110), (113), (024), (116), (214), and (300) planes of rhombohedral α-Al_2O_3 (JCPDS No. 98-004-0015). The absence of secondary reflections confirms its high crystallinity and phase purity. Similarly, the XRD pattern of the Cu/Al_2O_3 nanocomposite (Figure 1a, olive line) reveals diffraction peaks corresponding to face-centered cubic (FCC) Cu NPs [39]. The average crystallite size, calculated using the Scherrer equation, was found to be approximately 27.8 ± 2.5 nm. A slight shift in the 2θ values of Al_2O_3 was observed, which is likely due to the incorporation of Cu nanoparticles.

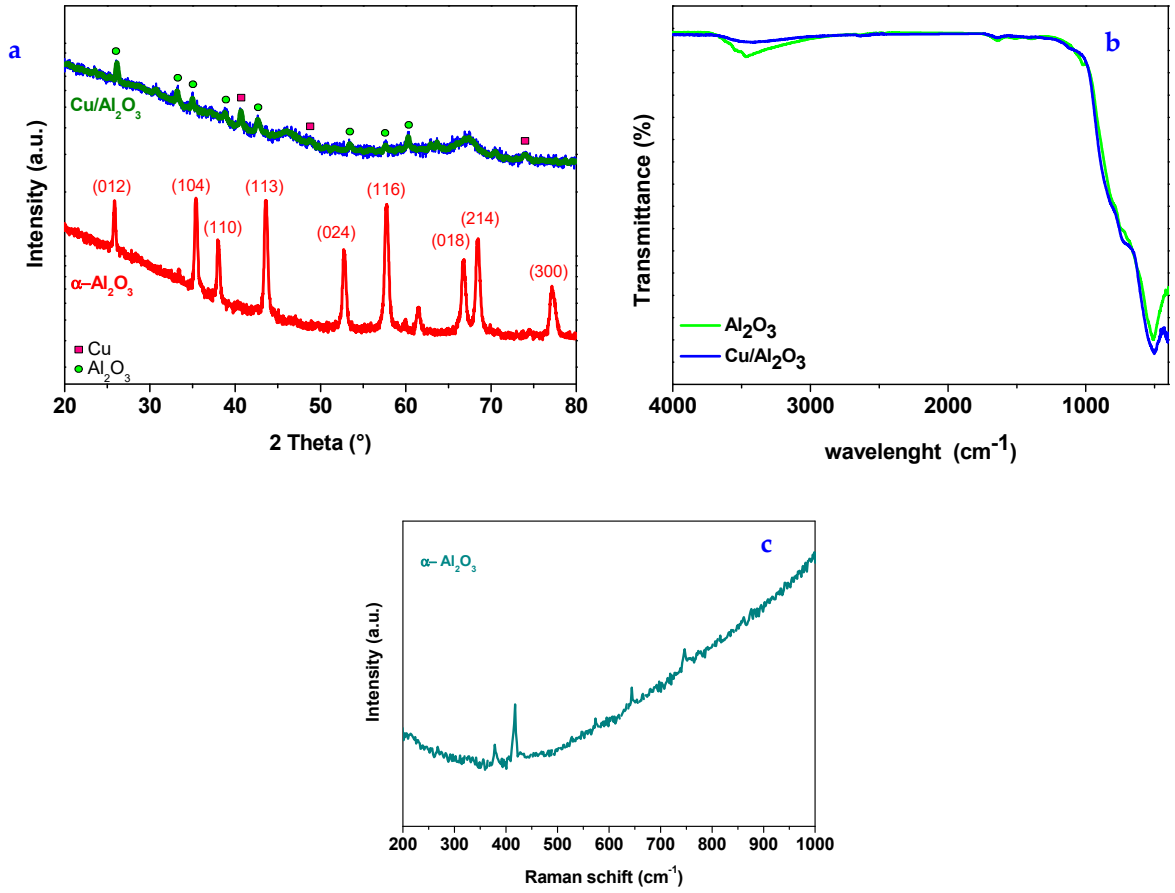


Figure 1. (**a**) XRD of Al_2O_3 NPs and Cu/Al_2O_3 NPs; (**b**) FT-IR profiles of Al_2O_3 NPs and Cu/Al_2O_3 NPs; (**c**) Raman spectrum of α-Al_2O_3.

The nature of the chemical bonds of the synthesized nanocomposites was investigated by FT-IR spectroscopy, which enabled the identification of surface functional groups.

Figure 1b presents the FT-IR spectra of pure α-Al_2O_3 and the Cu/Al_2O_3 composite material. Pure α-Al_2O_3 is typically characterized by absorption bands in the 500–800 cm^{-1} range, corresponding to the Al–O-Al stretching vibration [40]. The IR spectrum of Cu/Al_2O_3 nanoparticles shows the characteristic peaks of Al–O-Al stretching. The broad band centered at 3431 cm^{-1} is associated with the stretching vibrations of –OH groups and adsorbed water molecules, while the bands in the 1500–1700 cm^{-1} range are attributed to bending vibrations of species adsorbed on the material surface [41]. The Raman spectrum of the α-Al_2O_3 sample under excitation of 514 nm is also reported in Figure 1. In particular, Figure 1c shows the characteristic vibrational modes of α-alumina (α-Al_2O_3) nanoparticles, with Raman bands detected at 378, 415, 572, 643, and 746 cm^{-1}. These frequencies correspond to the active Raman modes A_1g (around 415 and 643 cm^{-1}) and E_9 (approximately 378, 415, 572, and 746 cm^{-1}) [42–44].

The XPS spectra of Cu/Al_2O_3 NPs are illustrated in Figure 2. As shown in Figure 2a, the XPS survey scan revealed characteristic peaks corresponding to Cu 2p, Al 2p, and O 1s. The spectra were calibrated using the C 1s peaks at 284.8 eV as reference. Specifically, in Figure 2b, the Al 2p binding energy is observed at approximately 73.9 eV, confirming the presence of aluminum in the +3 oxidation state (Al^{3+}) [45]. Figure 2c displays two distinct peaks at 932.3 eV and 952.7 eV, both assigned to Cu(0), confirming the presence of metallic copper species on the catalyst surface [46]. To exclude the occurrence of additional copper species, the O 1s spectrum was deconvoluted (Figure 2d), revealing two peaks centered at 530 eV and 532 eV. These features are attributed to lattice oxygen associated with aluminum (Al–O bonds) and Al–O–H bonds, respectively [47]. Overall, these spectroscopic results confirm the successful synthesis of Cu/Al_2O_3 nanoparticles with metallic copper species supported on alumina.

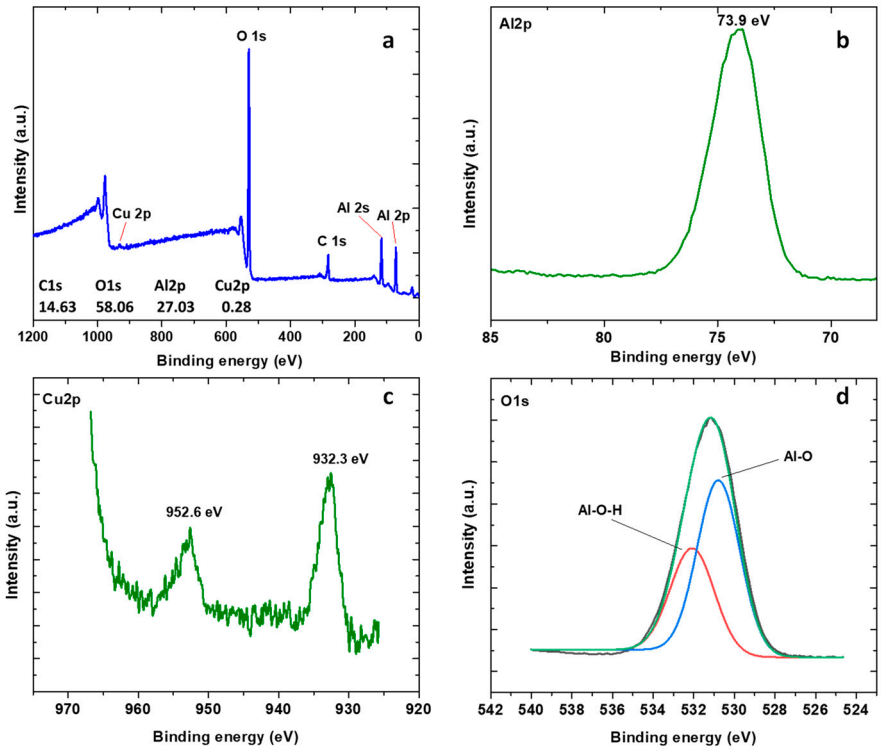


Figure 2. XPS spectra of Cu/Al_2O_3: XPS survey spectrum (**a**); Al 2p (**b**), Cu 2p (**c**), and O 1s (**d**) spectra.

Figure 3a,b displays the surface morphology of Cu/Al_2O_3 NPs, characterized by a relatively rough texture and the absence of a regular surface relief. Additionally, some particle agglomerates were observed on the surface of the sample. Specifically, Figure 3b displays

cluster-like structures with globular morphology, attributable to both the copper matrix and the alumina support (Figure 3c). The TEM inset in Figure 3c shows Al_2O_3-supported Cu NPs with irregular morphologies and an average particle size of approximately 65 nm, exhibiting a broad size distribution from 50 to 100 nm.

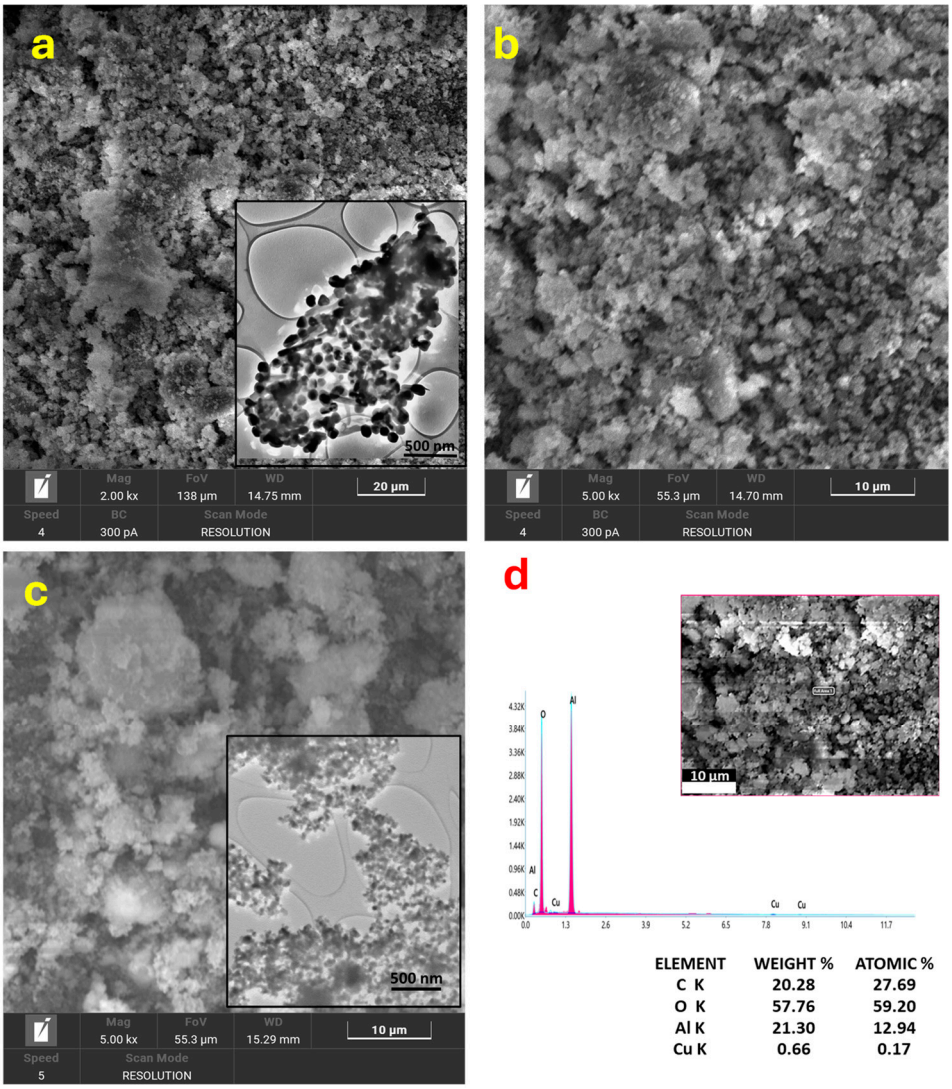


Figure 3. SEM images of Cu/Al_2O_3 NPs (**a**,**b**); TEM image of Cu/Al_2O_3 (inset (**a**)); SEM image of α-Al_2O_3 support (**c**); TEM image of α-Al_2O_3 (inset (**c**)); and EDX spectrum of Cu/Al_2O_3 NPs (**d**).

Finally, energy-dispersive X-ray spectroscopy (EDX) analysis confirmed the elemental composition of the material, namely aluminum (Al), oxygen (O), and copper (Cu), as shown in Figure 3d.

3.2. Tribo-Catalytic Efficiency of Cu/Al_2O_3 NPs

Tribo-catalysis induced by magnetic stirring using Cu/Al_2O_3 was investigated for the removal of MO as a model pollutant. Under continuous stirring at 500 rpm with a PTFE-coated magnetic bar in the presence of Cu/Al_2O_3, and in the absence of light, a gradual discoloration of the MO solution was observed. After 10 h of treatment, the solution was almost completely decolorized (95%), whereas alumina alone achieved only ~60% decolorization (see Figure 4a). In addition, when Cu nanoparticles alone were tested for MO degradation, only 41% removal was achieved after 10 h. Finally, to verify the tribo-catalytic activity of Cu/Al_2O_3 nanoparticles, a control experiment was performed in the absence

of the catalyst (Figure 4a). Under these conditions, no degradation of MO was observed, and the slight decrease in concentration can be considered negligible, likely resulting from the mere friction between the PTFE rod and the glass beaker. These findings confirm that the presence of the catalyst is essential for the activation of the tribo-catalytic process. The relative concentration (C/C_0) of MO was evaluated as a function of stirring time, where C and C_0 correspond to the instantaneous and initial concentrations, respectively. As shown in Figure 4, more than 95% of MO was degraded within 10 h in the presence of Cu/Al_2O_3 nanoparticles. Kinetic analysis based on the pseudo-first-order model, Equation (2),

$$\ln\left(\frac{C}{C_0}\right) = -kt \quad (2)$$

confirmed an excellent linear fit (Figure 4b), indicating that MO degradation proceeds via pseudo-first-order kinetics, with an apparent rate constant of 0.318 h^{-1}. This behavior is further supported by the evolution of the UV–Vis spectra of the MO solution over time (Figure 4c,d). The gradual decrease in the intensity of the characteristic absorption peak at around 464 nm, with no significant spectral shifts, indicates the progressive degradation of the dye via cleavage of the azo bond.

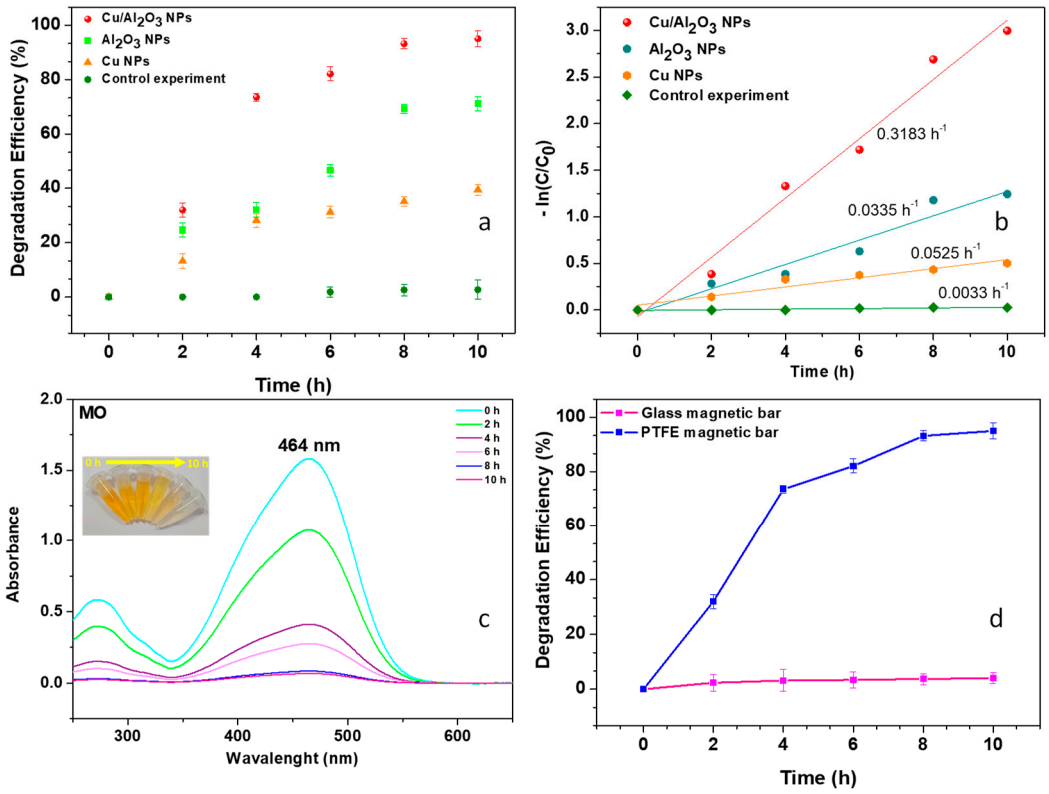


Figure 4. (**a**) Effect of the catalyst on the tribo-catalytic degradation of MO as a function of stirring time; (**b**) kinetic fitting for different catalysts; (**c**) UV–Vis spectral evolution of the MO solution under magnetic stirring (inset photo of the degradation of MO as a function of time); (**d**) effect of the material of magnetic bar on the tribo-catalytic degradation of MO. Reaction conditions: MO concentration: 20 mg/L; Cu/Al_2O_3 nanoparticles: 50 mg; pH: 6; temperature: room temperature; stirring speed: 500 rpm and dark conditions. The experimental data are based on three repeated experiments.

Moreover, the disappearance of absorption bands in the UV region, together with the absence of new signals, suggests that the aromatic structures of MO were broken down and converted into simpler molecular species. To confirm the role of the magnetic bar, the effect of the material was also evaluated. Using a glass bar, the degradation rate after 10 h

was only 4.01%, due to the limited electron transfer. In contrast, PTFE proved to be crucial; its low Fermi energy level enables substantial charge transfer with a high-Fermi-energy catalyst [48–52]. Operational parameters such as stirring speed and the contact area of magnetic bars significantly influence the efficiency of the tribo-catalytic process, as they affect the frictional dynamics between the materials involved. To evaluate this effect, the tribo-catalytic performance of Cu/Al_2O_3 was studied over a stirring speed range from 100 to 700 rpm (Figure 5).

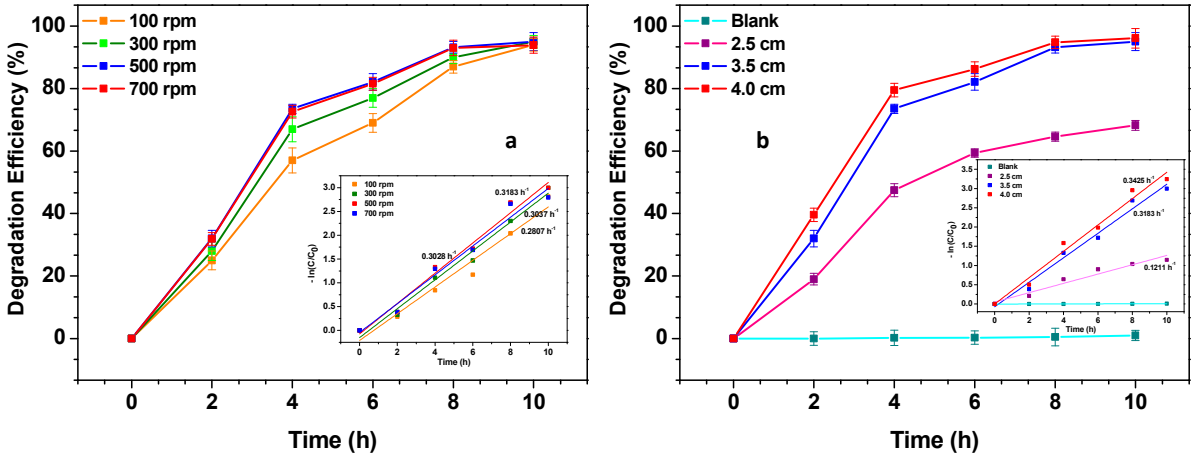


Figure 5. Tribo-catalytic performance of Cu/Al_2O_3 nanoparticles (NPs) for the degradation of methyl orange (MO): (**a**) effect of magnetic stirring rate (inset kinetic fitting); and (**b**) effect of PTFE magnetic rod length (inset kinetic fitting). Reaction conditions: MO concentration: 20 mg/L; Cu/Al_2O_3 NPs: 50 mg; pH: 6; temperature: room temperature and dark conditions.

An increase in stirring speed leads to more frequent and intense collisions between the catalyst and methyl orange (MO) molecules, thereby promoting the generation of reactive species and accelerating dye degradation. As shown in Figure 5a, the MO removal efficiency increases with stirring speed. This behavior is attributed to the higher number of frictional contacts per unit time between Cu/Al_2O_3 particles and the surface of the PTFE-coated magnetic stirring bar. The intensified friction facilitates the cleavage of azo bonds in the MO molecular structure, thereby improving the overall degradation process. Furthermore, the tribo-catalytic performance of Cu/Al_2O_3 particles slightly decreased when the stirring speed was increased to 700 rpm, which may be attributed to the partial dispersion of catalyst particles onto the beaker walls at higher stirring rates. All experiments were carried out in the dark to exclude any contribution from photocatalysis. Moreover, the effectiveness of the tribo-catalytic process is strongly influenced not only by stirring speed but also by the friction generated and the contact area between the magnetic stirring bar and the bottom of the beaker. A larger contact area between the PTFE-coated magnetic bar and the glass surface promotes the accumulation of Cu/Al_2O_3 particles at the solid–solid interface, thereby intensifying the catalytic activity through tribo-electric mechanisms. To experimentally investigate this effect, magnetic bars of different lengths were employed (Figure 5b). Increasing the bar length from 2.5 to 4.0 cm led to a pronounced enhancement in the degradation efficiency of methyl orange (MO), highlighting the critical role of contact area in tribo-catalytic activation. However, extending the length from 3.5 to 4.0 cm resulted in only a marginal improvement. Overall, these findings confirm that tribo-catalytic performance is positively correlated with contact area, although the incremental benefits tend to diminish beyond a certain threshold.

To further support this observation, a blank experiment was conducted in the absence of the magnetic bar. Under these conditions, no degradation of MO was observed,

demonstrating that the mere presence of the catalyst is not sufficient. Mechanical friction generated by the movement of the PTFE-coated magnetic bar is crucial for triggering the tribo-catalytic process.

The effect of pH on the tribo-catalytic degradation of MO dye using the Cu/Al_2O_3 catalyst was systematically investigated at approximately pH 3, 6, and 9. The pH of the dye solutions was adjusted with 0.1 M NaOH or 0.1 M HCl to cover acidic, neutral, and alkaline conditions. At acidic pH values, the catalyst surface becomes positively charged, leading to electrostatic repulsion with the cationic form of MO, whereas under near-neutral conditions, attractive interactions occur with the anionic dye species. In contrast, at alkaline pH, the surface turns negatively charged, again causing repulsion with the anionic MO. These variations in surface charge and dye–catalyst interactions affect the adsorption process and, consequently, the efficiency of tribo-catalytic degradation. Neutral pH conditions, around 6, were identified as optimal. The effect of catalyst dosage on tribo-catalytic degradation performance is presented in Figure 6b. The Cu/Al_2O_3 catalyst demonstrates a progressive enhancement in the degradation of MO dye as the concentration increases from 10 mg/30 mL to 50 mg/30 mL. This improvement can be ascribed to the larger contact area established between Cu/Al_2O_3 particles and the stirrer, since a higher number of catalyst particles interact with the stirrer at increased dosages. As a result, the generation of active radicals is promoted, which is likely the key factor contributing to the enhanced degradation efficiency.

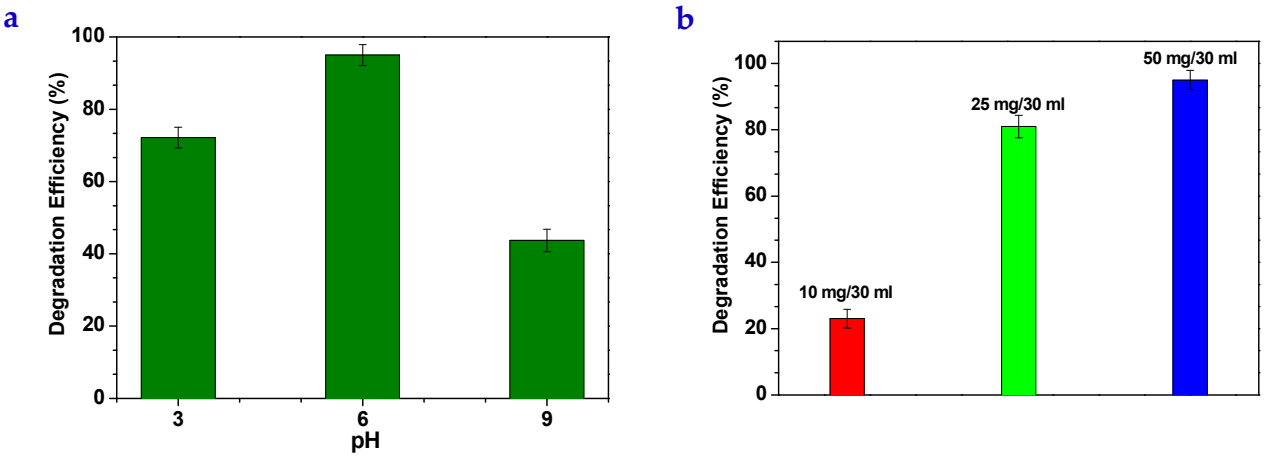


Figure 6. Tribo-catalytic performance of Cu/Al_2O_3 NPs for the degradation of MO: (**a**) effect of pH. Reaction conditions: MO concentration: 20 mg/L; Cu/Al_2O_3 NPs: 50 mg; time: 10 h; stirring speed: 500 rpm; temperature: room temperature and dark conditions; (**b**) effect of catalyst dose concentration. Reaction conditions: MO concentration: 20 mg/L; pH: 6; time: 10 h; stirring speed: 500 rpm; temperature: room temperature and dark conditions.

3.3. Possible Mechanism for Tribo-Catalytic Degradation of MO

The degradation of MO was achieved using Cu/Al_2O_3 nanoparticles under magnetic stirring conditions (as shown in Figure 7). It is proposed that frictional interactions between the Cu/Al_2O_3 nanoparticles and the surfaces of the reaction vessel, namely, the PTFE-coated magnetic stir bar and the glass beaker, induce the excitation of electron–hole pairs within the catalyst material [53–57]. The generated charge carriers (electrons and holes) migrate to the surface of the catalyst and transfer into the surrounding aqueous solution, where they initiate redox reactions that result in the formation of reactive oxygen species (ROS) such as hydroxyl radicals (·OH) and superoxide radicals ($\cdot O_2^-$).

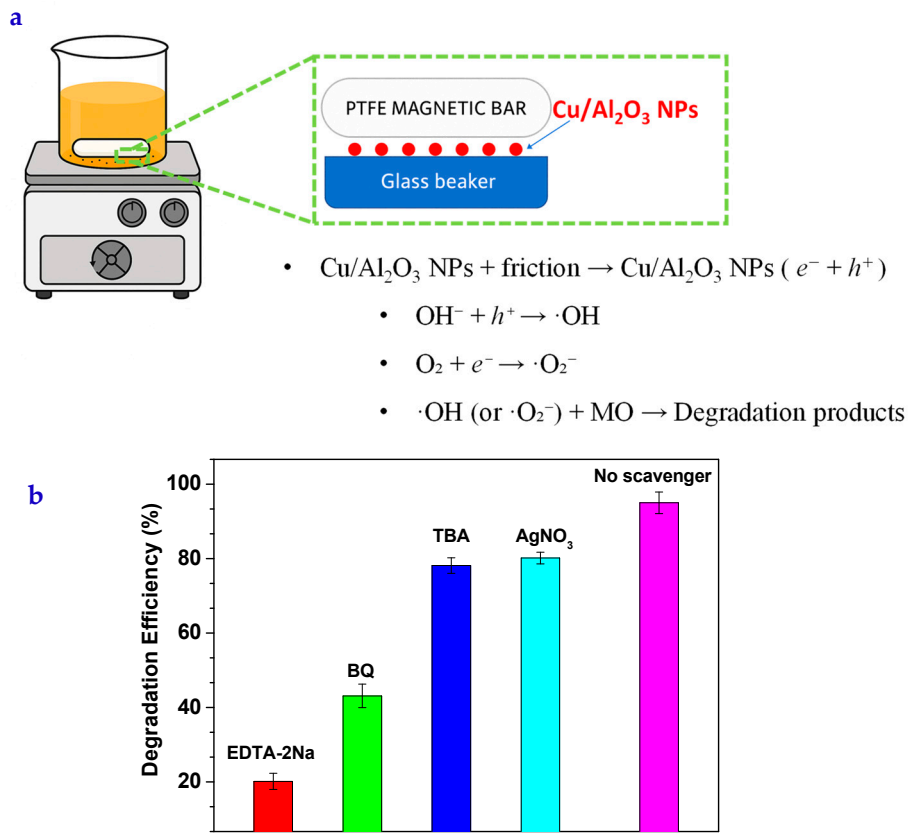


Figure 7. Schematic diagram of tribo-catalysis on Cu/Al_2O_3 NPs for degradation of MO (**a**); tribo-catalytic performance of Cu/Al_2O_3 NPs for the degradation of MO with the addition of various scavengers (**b**).

These highly reactive species are responsible for the oxidative degradation of MO dye molecules. The tribo-catalytic degradation mechanism can be summarized as follows:

$$Cu/Al_2O_3\ NPs + friction \rightarrow Cu/Al_2O_3\ NPs\ (e^- + h^+)$$

- Generation of hydroxyl radicals through hole-induced oxidation of hydroxide ions:

$$OH^- + h^+ \rightarrow \cdot OH$$

- Formation of superoxide radicals by electron transfer to dissolved oxygen:

$$O_2 + e^- \rightarrow \cdot O_2^-$$

- Oxidative attack on MO dye molecules by ROS:

$$OH\ (or\ \cdot O_2^-) + MO \rightarrow Degradation\ products$$

These findings demonstrate that Cu/Al_2O_3 acts as an effective tribo-catalyst, capable of converting mechanical frictional energy into chemical energy through the generation of redox-active species [58]. This highlights the significant potential of tribo-catalysis as a sustainable and efficient strategy for the degradation of organic pollutants and environmental remediation. On the other hand, to validate the proposed mechanism, reactive species trapping experiments were conducted. As shown in Figure 7b, the degradation efficiency of MO decreased upon the addition of specific scavengers, p-Benzoquinone (BQ; $\cdot O_2^-$), tert-butanol (TBA; ·OH), and silver nitrate ($AgNO_3$; e^-), while a pronounced inhibition

was observed with ethylenediaminetetraacetic acid disodium salt dihydrate (EDTA-2Na; h^+). The sequence of their effects followed the order of $h^+ > \cdot O_2^- > \cdot OH \approx e^-$, confirming that holes are the primary active species in the tribo-catalytic process, with $\cdot O_2^-$, ·OH, and e^- playing secondary roles.

3.4. Reusability of the Cu/Al_2O_3 Catalyst

Evaluating the long-term performance of the Cu/Al_2O_3 catalyst is essential for its practical application in environmental remediation. To this end, a reusability test was conducted using 30 mL of MO solution (20 mg/L), treated with 50 mg of Cu/Al_2O_3 under magnetic stirring (500 rpm) in the dark. Each tribo-catalytic cycle lasted 10 h. After each run, the catalyst was recovered, rinsed thoroughly with deionized water, and dried at 60 °C before reuse. As presented in Figure 8, the catalyst maintained high activity over five consecutive cycles, with MO degradation efficiency remaining at ~91%, compared to ~95% in the first cycle. This minimal performance loss highlights the excellent structural stability and reusability of Cu/Al_2O_3, underscoring its potential as a durable and scalable tribo-catalyst for repeated use in pollutant degradation systems. Table 1 summarizes a head-to-head comparison of dye-degradation efficiencies across different catalysts and dyes. The catalyst developed in this work is inexpensive, easily reusable, and simple to synthesize, showing superior performance compared with many literature-reported systems and highlighting its promise for tribo-catalytic environmental remediation.

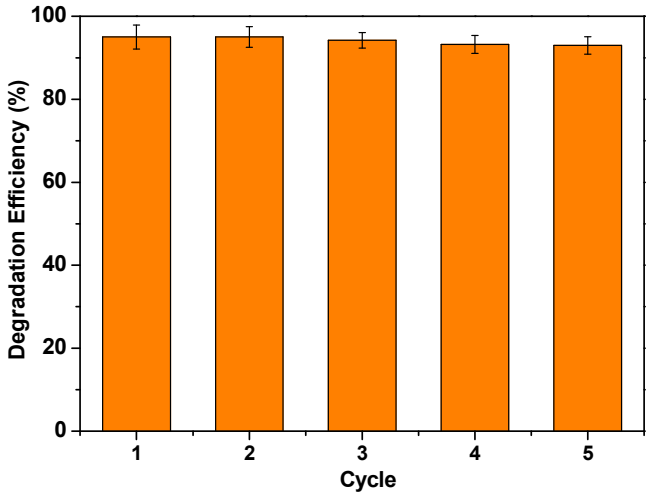


Figure 8. Reusability of Cu/Al_2O_3 NPs for the tribo-catalytic degradation of MO over five consecutive cycles. Reaction conditions: MO concentration: 20 mg/L; Cu/Al_2O_3 NPs: 50 mg; stirring speed: 500 rpm; temperature: room temperature; dark conditions; duration per cycle: 10 h; pH: 6.

Table 1. Comparison with the literature on tribo-catalytic degradation of organic dyes.

Catalysts	Dosage (mg/L)	Pollutants	Stirring Speed (rpm)	Degradation (%)	Degradation Time (h)	Kinetic Rate (h^{-1})	Cycle Degradation	Ref.
$Ba(Zr_{0.05}Ti_{0.95})O_3$	50	RhB 5 mg/L	1200	94.3	6	0.4482	3 (92%)	[59]
$Ba_{0.8}Sr_{0.2}TiO_3$	30	RhB 5 mg/L	400	88.0	8	0.2613	3 (83%)	[60]
$BaSrTiO_3$ NPs	30	MO 5 mg/L	300	80.0	24	-	-	[61]
$BiOIO_3$	30	RhB 5 mg/L	500	98.5	12	0.3760	5 (96%)	[27]
CdS nanowires	30	RhB 10 mg/L	400	98.0	7	0.3200	5 (95%)	[62]
$NiCo_2O_4$	30	RhB 5 mg/L	400	98.6	56	0.0740	10 (91%)	[63]
PTFE	30	RhB 5 mg/L	500	97.0	12	0.0056	5 (90%)	[64]
Cu/Al_2O_3	50	MO 20 mg/L	500	95.0	10	0.3183	5 (91%)	This work

On the other hand, Table 2 highlights different copper-based catalytic approaches for organic pollutant removal. Cu-oxide catalysts (e.g., Sm_2CuO_4) are efficient under

visible-light photocatalysis, while Cu-based electrodes (e.g., Cu) achieve high performance in electrocatalysis. Moreover, Fenton-like systems (Cu@SB) and persulfate activation ($CuFe_2O_4$@GO) also demonstrate high efficiency. Finally, supported Cu/Al_2O_3 illustrates how tribo-catalysis can achieve a high performance (95%) and may represent a possible sustainable alternative, as it does not require light or external oxidants, and thus can emerge as a sustainable route for dye degradation.

Table 2. Copper-based catalytic technologies for pollutant removal.

Technologies	Catalyst	Pollutants	Efficiency (%)	Ref.
Photocatalysis	Sm_2CuO_4 nanostructures	MO	91.4	[65]
Electrocatalysis	Cu electrode	MO	100	[66]
Fenton-like	Cu@SB nanozyme	Amlodipine	100	[67]
PMS activation	$CuFe_2O_4$@GO	Dyes	>90	[68]
Tribo-catalyst	Cu/Al_2O_3	MO	95	This work

4. Conclusions

This work demonstrated, for the first time, the tribo-catalytic efficiency of Cu/Al_2O_3 nanoparticles for the degradation of methyl orange (MO), utilizing only mechanical energy generated by magnetic stirring under ambient conditions and in the absence of light. The system achieved a remarkable 95% degradation of MO within 10 h, significantly outperforming pure α-Al_2O_3, which reached only 60% under the same conditions. The tribo-catalytic performance was strongly influenced by the stirring speed and the contact area between the PTFE-coated magnetic stir bar and the vessel surface. Increasing the stirring rate from 100 to 500 rpm and using longer magnetic bars (from 2.5 cm to 3.5 cm) notably enhanced dye removal efficiency by intensifying frictional interactions and tribo-electric charge generation. Control experiments confirmed that MO degradation was negligible in the absence of the catalyst or without mechanical stirring, ruling out contributions from photodegradation or spontaneous breakdown. Furthermore, the Cu/Al_2O_3 catalyst maintained high catalytic activity over five consecutive cycles, with only a slight decrease in performance from 95% to 91%, confirming its excellent structural stability and reusability. These findings highlight the potential of Cu/Al_2O_3 as an effective, robust, and sustainable tribo-catalyst for environmental remediation, particularly in the treatment of wastewater containing persistent organic pollutants.

Author Contributions: Conceptualization, C.C. and M.I.; Methodology, C.C., M.I. and S.A.; Validation, C.C. and M.I.; Formal Analysis, C.C., M.I. and E.N.A.; Investigation, C.C., M.I., S.A. and E.N.A. Data Curation, C.C., M.I. and E.N.A.; Writing—Original Draft Preparation, C.C. and M.I.; Writing—Review and Editing, C.C., M.I., E.N.A. and M.S.; Visualization, C.C., M.I., E.N.A., S.A. and M.S.; Supervision, E.N.A. and M.S. All authors have read and agreed to the published version of the manuscript.

Funding: This research received no external funding.

Data Availability Statement: The data presented in this study are available on request from the author.

Conflicts of Interest: The authors declare no conflicts of interest.

References

1. Xiao, L.; Xu, X.; Wu, Z.; Sun, T.; He, X.; Xu, X.; Qin, L.; Chen, D. Recent progress and prospect of friction-driven-tribocatalysis: From basic principle to material design. *Surf. Interfaces* **2024**, *56*, 105557. [CrossRef]
2. Li, X.; Tong, W.; Shi, J.; Chen, Y.; Zhang, Y.; An, Q. Tribocatalysis mechanisms: Electron transfer and transition. *J. Mater. Chem. A* **2023**, *11*, 4458–4472. [CrossRef]

3. Sun, C.; Guo, X.; Hu, C.; Liu, L.; Fang, L.; Cheng, Z.; Luo, N. Tribocatalytic degradation of dyes by tungsten bronze ferroelectric $Ba_{2.5}Sr_{2.5}Nb_8Ta_2O_{30}$ submicron particles. *RSC Adv.* **2021**, *11*, 13386–13395. [CrossRef]
4. Wu, M.; Zhang, Y.; Yi, Y.; Zhou, B.; Sun, P.; Dong, X. Regulation of friction pair to promote conversion of mechanical energy to chemical energy on Bi_2WO_6 and realization of enhanced tribocatalytic activity to degrade different pollutants. *J. Hazard. Mater.* **2023**, *459*, 132147. [CrossRef]
5. Yuan, A.; Lei, H.; Xi, F.; Liu, J.; Qin, L.; Chen, Z.; Dong, X. Graphene quantum dots decorated graphitic carbon nitride nanorods for photocatalytic removal of antibiotics. *J. Colloid Interface Sci.* **2019**, *548*, 56–65. [CrossRef]
6. Yao, C.; Yuan, A.; Zhang, H.; Li, B.; Liu, J.; Xi, F.; Dong, X. Facile surface modification of textiles with photocatalytic carbon nitride nanosheets and the excellent performance for self-cleaning and degradation of gaseous formaldehyde. *J. Colloid Interface Sci.* **2018**, *533*, 144–153. [CrossRef]
7. Henríquez, R.; Nogales, P.S.; Moreno, P.G.; Cartagena, E.M.; Bongiorno, P.L.; Navarrete-Astorga, E.; Dalchiele, E.A. One-Step hydrothermal synthesis of Cu_2ZnSnS_4 nanoparticles as an efficient visible light photocatalyst for the degradation of Congo Red Azo dye. *Nanomaterials* **2023**, *13*, 1731. [CrossRef] [PubMed]
8. Henríquez, R.; Nogales, P.S.; Moreno, P.G.; Cartagena, E.M.; Bongiorno, P.L.; Garate, P.Z.; Navarrete-Astorga, E.; Dalchiele, E.A. Solvothermal synthesis of $Cu_2ZnSnSe_4$ nanoparticles and their Visible-Light-Driven photocatalytic activity. *Nanomaterials* **2024**, *14*, 1079. [CrossRef] [PubMed]
9. Wu, J.; Qin, N.; Bao, D. Effective enhancement of piezocatalytic activity of $BaTiO_3$ nanowires under ultrasonic vibration. *Nano Energy* **2017**, *45*, 44–51. [CrossRef]
10. Wu, J.M.; Sun, Y.; Chang, W.; Lee, J. Piezoelectricity induced water splitting and formation of hydroxyl radical from active edge sites of MoS_2 nanoflowers. *Nano Energy* **2018**, *46*, 372–382. [CrossRef]
11. Shao, Y.; Shen, M.; Zhou, Y.; Cui, X.; Li, L.; Zhang, Y. Nanogenerator-based self-powered sensors for data collection. *Beilstein J. Nanotechnol.* **2021**, *12*, 680–693. [CrossRef]
12. You, H.; Jia, Y.; Wu, Z.; Xu, X.; Qian, W.; Xia, Y.; Ismail, M. Strong piezo-electrochemical effect of multiferroic $BiFeO_3$ square micro-sheets for mechanocatalysis. *Electrochem. Commun.* **2017**, *79*, 55–58. [CrossRef]
13. Hong, K.; Xu, H.; Konishi, H.; Li, X. Piezoelectrochemical Effect: A New Mechanism for Azo Dye Decolorization in Aqueous Solution through Vibrating Piezoelectric Microfibers. *J. Phys. Chem. C* **2012**, *116*, 13045–13051. [CrossRef]
14. Tian, J.; He, Y.; Li, F.; Peng, W.; He, Y. On the mechanism of contact electrification: A comprehensive review. *J. Mater. Chem. A* **2024**, *15*, 2505–2536. [CrossRef]
15. Che, J.; Gao, Y.; Wu, Z.; Ma, J.; Wang, Z.; Liu, C.; Jia, Y.; Wang, X. Review on tribocatalysis through harvesting friction energy for mechanically-driven dye decomposition. *J. Alloys Compd.* **2024**, *1002*, 175413. [CrossRef]
16. Zhao, B.; Chen, N.; Xue, Y.; Shi, H.; Xu, H.; Li, M.; Sun, C.; Xing, Y.; Gao, B.; Ma, B. Challenges and perspectives of tribocatalysis in the treatment for dye wastewater. *J. Water Process Eng.* **2024**, *63*, 105455. [CrossRef]
17. Iuliano, M.; Cirillo, C.; Astorga, E.N.; Sarno, M. A new nanocomposite as adsorbent and catalyst for enhanced removal of methylene blue. *Surf. Interfaces* **2024**, *51*, 104582. [CrossRef]
18. Iuliano, M.; Ponticorvo, E.; Cirillo, C.; Sarno, M. A New Nanocomposite from Vesuvian Slope Pinecones for Azo-Dyes Removal. *Ind. Eng. Chem. Res.* **2022**, *61*, 1965–1976. [CrossRef]
19. Zafar, S.; Bukhari, D.A.; Rehman, A. Azo dyes degradation by microorganisms—An efficient and sustainable approach. *Saudi J. Biol. Sci.* **2022**, *29*, 103437. [CrossRef] [PubMed]
20. Iuliano, M.; Ponticorvo, E.; Cirillo, C.; Adami, R.; Sarno, M. Catalytic hydrogenation of organic dyes by Ag and Au magnetic nanoparticles supported on nanocellulose from waste pistachio shells. *Mol. Catal.* **2023**, *544*, 113179. [CrossRef]
21. Forgacs, E.; Cserháti, T.; Oros, G. Removal of synthetic dyes from wastewaters: A review. *Environ. Int.* **2004**, *30*, 953–971. [CrossRef]
22. Gu, Y.; Zhang, W.; Li, Y.; Wang, K.; Ge, L.; Zhang, X.; Zhao, J.; Shen, Z.; Chen, W.; Hu, Y. Tribocatalytic degradation of concentrated methyl orange solutions by $BiFeO_3$ nanoparticles prepared through a sol–gel method. *RSC Adv.* **2025**, *15*, 23089–23096. [CrossRef]
23. Kishor, R.; Purchase, D.; Saratale, G.D.; Ferreira, L.F.R.; Hussain, C.M.; Mulla, S.I.; Bharagava, R.N. Degradation mechanism and toxicity reduction of methyl orange dye by a newly isolated bacterium Pseudomonas aeruginosa MZ520730. *J. Water Process Eng.* **2021**, *43*, 102300. [CrossRef]
24. Cui, X.; Li, P.; Lei, H.; Tu, C.; Wang, D.; Wang, Z.; Chen, W. Greatly enhanced tribocatalytic degradation of organic pollutants by TiO_2 nanoparticles through efficiently harvesting mechanical energy. *Sep. Purif. Technol.* **2022**, *289*, 120814. [CrossRef]
25. Lei, H.; Cui, X.; Jia, X.; Qi, J.; Wang, Z.; Chen, W. Enhanced tribocatalytic degradation of organic pollutants by ZNO nanoparticles of high crystallinity. *Nanomaterials* **2022**, *13*, 46. [CrossRef]
26. Zhao, J.; Chen, L.; Luo, W.; Li, H.; Wu, Z.; Xu, Z.; Zhang, Y.; Zhang, H.; Yuan, G.; Gao, J.; et al. Strong tribo-catalysis of zinc oxide nanorods via triboelectrically-harvesting friction energy. *Ceram. Int.* **2020**, *46*, 25293–25298. [CrossRef]
27. Lei, H.; Wu, M.; Mo, F.; Ji, S.; Dong, X.; Wu, Z.; Gao, J.; Yang, Y.; Jia, Y. Tribo-catalytic degradation of organic pollutants through bismuth oxyiodate triboelectrically harvesting mechanical energy. *Nano Energy* **2020**, *78*, 105290. [CrossRef]

28. Gaur, A.; Moharana, A.K.; Porwal, C.; Chauhan, V.S.; Vaish, R. Degradation of organic dyes by utilizing $CaCu_3Ti_4O_{12}$ (CCTO) nanoparticles via tribocatalysis process. *J. Ind. Eng. Chem.* **2023**, *129*, 341–351. [CrossRef]
29. Zhu, M.; Song, J.; Ke, S.; Gu, Y.; Bing, L.; Shen, Z.; Chen, W. TI Coating-Enhanced tribocatalytic degradation of organic dyes by CDS nanoparticles. *Inorganics* **2025**, *13*, 46. [CrossRef]
30. Trueba, M.; Trasatti, S.P. Γ-Alumina as a support for Catalysts: A Review of Fundamental Aspects. *Eur. J. Inorg. Chem.* **2005**, *2005*, 3393–3403. [CrossRef]
31. Sun, Y.; Li, S.; Zhao, Q.; Cong, Z.; Xia, Y.; Jiao, X.; Chen, D. Recent advancements in Alumina-Based High-Temperature insulating Materials: Properties, applications, and future Perspectives. *High-Temp. Mater.* **2025**, *2*, 10001. [CrossRef]
32. Jähnichen, T.; Carstens, S.; Franz, M.; Laufer, O.; Wenzel, M.; Matysik, J.; Enke, D. Towards High Surface Area α-Al_2O_3–Mn-Assisted Low Temperature Transformation. *Materials* **2023**, *16*, 3047. [CrossRef] [PubMed]
33. Ke, S.; Mao, C.; Luo, R.; Zhou, Z.; Hu, Y.; Zhao, W.; Chen, W. Surprising effects of Al_2O_3 coating on tribocatalytic degradation of organic dyes by CDS nanoparticles. *Coatings* **2024**, *14*, 1057. [CrossRef]
34. Das, A.; Ren, Y.; Hessin, C.; Murr, M.D. Copper catalysis with redox-active ligands. *Beilstein J. Org. Chem.* **2020**, *16*, 858–870. [CrossRef]
35. Cui, X.; Wang, H.; Lei, H.; Jia, X.; Jiang, Y.; Fei, L.; Jia, Y.; Chen, W. Surprising Tribo-catalytic Conversion of H_2O and CO_2 into Flammable Gases utilizing Frictions of Copper in Water. *ChemistrySelect* **2023**, *8*, e202204146. [CrossRef]
36. Song, Y.; Chen, W.; Zhao, C.; Li, S.; Wei, W.; Sun, Y. Metal-Free Nitrogen-Doped mesoporous carbon for electroreduction of CO_2 to ethanol. *Angew. Chem. Int. Ed.* **2017**, *56*, 10840–10844. [CrossRef]
37. Chen, M.; Jia, Y.; Li, H.; Wu, Z.; Huang, T.; Zhang, H. Enhanced pyrocatalysis of the pyroelectric $BiFeO_3$/g-C_3N_4 heterostructure for dye decomposition driven by cold-hot temperature alternation. *J. Adv. Ceram.* **2021**, *10*, 338–346. [CrossRef]
38. Wu, Z.; Luo, W.; Zhang, H.; Jia, Y. Strong pyro-catalysis of shape-controllable bismuth oxychloride nanomaterial for wastewater remediation. *Appl. Surf. Sci.* **2020**, *513*, 145630. [CrossRef]
39. Putri, S.E.; Herawati, N.; Fudhail, A.; Pratiwi, D.E.; Side, S.; Rahman, A.; Desa, S.S.; Ahmad, N.; Junaedi, S.; Surleva, A. Biosynthesis of Copper Nanoparticles Using Hylocereus costaricensis Peel Extract and their Photocatalytic Properties. *Karbala Int. J. Mod. Sci.* **2023**, *9*, 13. [CrossRef]
40. Liu, C.; Shih, K.; Gao, Y.; Li, F.; Wei, L. Dechlorinating transformation of propachlor through nucleophilic substitution by dithionite on the surface of alumina. *J. Soils Sediments* **2012**, *12*, 724–733. [CrossRef]
41. Černík, M.; Padil, V.V.T. Green synthesis of copper oxide nanoparticles using gum karaya as a biotemplate and their antibacterial application. *Int. J. Nanomed.* **2013**, *8*, 889–898. [CrossRef] [PubMed]
42. Thanigachalam, S.; Pathak, M.; Sathiyanarayanan, K.I. Photodegradation of rhodamine-B and methyl orange employing nano-alumina developed from new aluminium(III) complex(es) associated with phenanthridine-salicylaldehyde derived ligands. *J. Coord. Chem.* **2022**, *75*, 2189–2213. [CrossRef]
43. Li, P.; Lei, M.; Tang, W. Raman and photoluminescence properties of α-Al_2O_3 microcones with hierarchical and repetitive superstructure. *Mater. Lett.* **2009**, *64*, 161–163. [CrossRef]
44. Aldbea, F.W.; Vazquez, C.V.; Abobaker, M.; Alsteeni, A.; Saad, A.; Sharma, A.; Singh, P.K.; Diantoro, M.; May, M.; Abdullah, T.; et al. Structural and Optical Properties of α Aluminum Oxide prepared by sol-gel method. *Curr. Appl. Phys.* **2024**, *71*, 85–90. [CrossRef]
45. Yan, J.; Li, J.; Peng, J.; Zhang, H.; Zhang, Y.; Lai, B. Efficient degradation of sulfamethoxazole by the CuO@Al_2O_3 (EPC) coupled PMS system: Optimization, degradation pathways and toxicity evaluation. *Chem. Eng. J.* **2018**, *359*, 1097–1110. [CrossRef]
46. Mondal, P.; Sinha, A.; Salam, N.; Roy, A.S.; Jana, N.R.; Islam, S.M. Enhanced catalytic performance by copper nanoparticle–graphene based composite. *RSC Adv.* **2013**, *3*, 5615. [CrossRef]
47. Fang, R.; Sun, Q.; Zhou, P.; Yang, W.; Wang, P.; Zhang, D.W. High-performance bilayer flexible resistive random access memory based on low-temperature thermal atomic layer deposition. *Nanoscale Res. Lett.* **2013**, *8*, 92. [CrossRef]
48. Zhang, X.; Chen, L.; Jiang, Y.; Lim, W.; Soh, S. Rationalizing the triboelectric series of polymers. *Chem. Mater.* **2019**, *31*, 1473–1478. [CrossRef]
49. Gallo, C.; Lama, W. Some charge exchange phenomena explained by a classical model of the work function. *J. Electrost.* **1976**, *2*, 145–150. [CrossRef]
50. Diaz, A.; Felix-Navarro, R. A semi-quantitative tribo-electric series for polymeric materials: The influence of chemical structure and properties. *J. Electrost.* **2004**, *62*, 277–290. [CrossRef]
51. Wu, J.; Wang, X.; Li, H.; Wang, F.; Yang, W.; Hu, Y. Insights into the mechanism of metal-polymer contact electrification for triboelectric nanogenerator via first-principles investigations. *Nano Energy* **2018**, *48*, 607–616. [CrossRef]
52. Zhao, P.; Bhattacharya, G.; Fishlock, S.J.; Guy, J.G.; Kumar, A.; Tsonos, C.; Yu, Z.; Raj, S.; McLaughlin, J.A.; Luo, J.; et al. Replacing the metal electrodes in triboelectric nanogenerators: High-performance laser-induced graphene electrodes. *Nano Energy* **2020**, *75*, 104958. [CrossRef]

53. Geng, L.; Qian, Y.; Song, W.; Bao, L. Enhanced tribocatalytic pollutant degradation through tuning oxygen vacancy in $BaTiO_3$ nanoparticles. *Appl. Surf. Sci.* **2023**, *637*, 157960. [CrossRef]
54. Schwab, T.; Thomele, D.; Aicher, K.; Dunlop, J.W.C.; McKenna, K.; Diwald, O. Rubbing powders: Direct spectroscopic observation of triboinduced oxygen radical formation in MGO nanocube ensembles. *J. Phys. Chem. C* **2021**, *125*, 22239–22248. [CrossRef]
55. Alabbad, E.A.; Bashir, S.; Liu, J.L. Efficient removal of direct yellow dye using chitosan crosslinked isovanillin derivative biopolymer utilizing triboelectric energy produced from homogeneous catalysis. *Catal. Today* **2021**, *400–401*, 132–145. [CrossRef]
56. Cui, X.; Guo, Z.; Lei, H.; Jia, X.; Mao, C.; Ruan, L.; Zhou, X.; Wang, Z.; Chen, F.; Chen, W. Tribo-Catalytic degradation of methyl orange solutions enhanced by silicon single crystals. *Coatings* **2023**, *13*, 1804. [CrossRef]
57. Li, J.; Xu, X. Catalytic degradation of organic dyes induced by Tribo-Electrification between insulating films. *Materials* **2025**, *18*, 2327. [CrossRef]
58. Park, J.Y.; Salmeron, M. Fundamental aspects of energy dissipation in friction. *Chem. Rev.* **2014**, *114*, 677–711. [CrossRef]
59. Tang, Q.; Zhu, M.D.; Zhang, H.F.; Gao, J.; Kwok, K.W.; Kong, L.B.; Jia, Y.M.; Liu, L.J.; Peng, B.L. Enhanced tribocatalytic degradation of dye pollutants through governing the charge accumulations on the surface of ferroelectric barium zirconium titanate particles. *Nano Energy* **2022**, *100*, 107519. [CrossRef]
60. Liu, S.Y.; Yang, Y.D.; Hu, Y.M.; Rao, W.F. Effect of strontium substitution on the tribocatalytic performance of barium titanate. *Materials* **2023**, *16*, 3160. [CrossRef]
61. Li, P.; Wu, J.; Wu, Z.; Jia, Y.; Ma, J.; Chen, W.; Zhang, L.; Yang, J.; Liu, Y. Strong tribocatalytic dye decomposition through utilizing triboelectric energy of barium strontium titanate nanoparticles. *Nano Energy* **2019**, *63*, 103832. [CrossRef]
62. Yang, B.A.; Chen, H.B.; Guo, X.D.; Wang, L.; Xu, T.; Bian, J.H.; Yang, Y.D.; Liu, Q.D.; Du, Y.P.; Lou, X.J. Enhanced tribocatalytic degradation using piezoelectric CdS nanowires for efficient water remediation. *J. Mater. Chem. C* **2020**, *8*, 14845–14854. [CrossRef]
63. Ruan, L.J.; Jia, Y.M.; Guan, J.F.; Xue, B.; Huang, S.H.; Wang, Z.H.; Fu, Y.H.; Wu, Z. Tribo-electro-catalytic dye degradation driven by mechanical friction using MOF-derived $NiCo_2O_4$ double-shelled nanocages. *J. Clean. Prod.* **2022**, *345*, 131060. [CrossRef]
64. Wang, Y.; Arandiyan, H.; Scott, J.; Bagheri, A.; Dai, H.X.; Amal, R. Recent advances in ordered meso/macroporous metal oxides for heterogeneous catalysis: A review. *J. Mater. Chem. A* **2017**, *5*, 8825–8846. [CrossRef]
65. Yousefzadeh, F.; Ghanbari, M.; Salavati-Niasari, M. Sonochemical synthesis and characterization of Sm_2CuO_4 nanostructures and their application as visible-light photocatalyst for degradation of water-soluble organic pollutants. *Chemosphere* **2023**, *338*, 139564. [CrossRef]
66. Sarfo, D.K.; Kaur, A.; Marshall, D.L.; O'Mullane, A.P. Electrochemical degradation and mineralisation of organic dyes in aqueous nitrate solutions. *Chemosphere* **2023**, *316*, 137821. [CrossRef]
67. Gong, Z.; Wang, J.; Shao, S.; Fan, B.; Shi, Y.; Qian, L.; Lu, K.; Gao, S. H_2O_2 activation over Cu-Schiff bases nanozyme for the removal of amlodipine: Kinetics, mechanism and toxicity evaluation. *Sep. Purif. Technol.* **2023**, *311*, 123329. [CrossRef]
68. Lei, X.; You, M.; Pan, F.; Liu, M.; Yang, P.; Xia, D.; Li, Q.; Wang, Y.; Fu, J. $CuFe_2O_4$@GO nanocomposite as an effective and recoverable catalyst of peroxymonosulfate activation for degradation of aqueous dye pollutants. *Chin. Chem. Lett.* **2019**, *30*, 2216–2220. [CrossRef]

Disclaimer/Publisher's Note: The statements, opinions and data contained in all publications are solely those of the individual author(s) and contributor(s) and not of MDPI and/or the editor(s). MDPI and/or the editor(s) disclaim responsibility for any injury to people or property resulting from any ideas, methods, instructions or products referred to in the content.